

Article

Effect of In-Plane Magnetic Field on Skyrmions in a Centrosymmetric Triangular-Lattice System with Symmetric Anisotropic Exchange Interaction

Satoru Hayami

Graduate School of Science, Hokkaido University, Sapporo 060-0810, Japan; hayami@phys.sci.hokudai.ac.jp

Abstract: We report our numerical results on the stability of the skyrmion crystal phase in an external magnetic field for both in-plane and out-of-plane directions in a centrosymmetric host. We analyze a spin model with the two-spin symmetric anisotropic exchange interaction that arises from relativistic spin–orbit coupling on a triangular lattice. By performing simulated annealing, we construct magnetic phase diagrams when the magnetic field is tilted from the out-of-plane field direction to the in-plane field direction. We find a different stability tendency of the skyrmion crystal phase according to the directions of the in-plane field, which provides a signal of the two-spin symmetric anisotropic exchange interaction for stabilizing the skyrmion crystal phase. Our results indicate that the mechanism of the skyrmion crystal phase triggered by the two-spin symmetric anisotropic exchange interaction can be experimentally tested by applying the in-plane magnetic field.

Keywords: skyrmion crystal; multiple- Q magnetic state; triangular lattice; bond-dependent symmetric anisotropic interaction



Citation: Hayami, S. Effect of In-Plane Magnetic Field on Skyrmions in a Centrosymmetric Triangular-Lattice System with Symmetric Anisotropic Exchange Interaction. *Magnetism* **2024**, *4*, 54–72. <https://doi.org/10.3390/magnetism4010005>

Academic Editor: Giancarlo Consolo

Received: 7 February 2024

Revised: 26 February 2024

Accepted: 12 March 2024

Published: 18 March 2024



Copyright: © 2024 by the author. Licensee MDPI, Basel, Switzerland. This article is an open access article distributed under the terms and conditions of the Creative Commons Attribution (CC BY) license (<https://creativecommons.org/licenses/by/4.0/>).

1. Introduction

A multiple- Q spin texture, consisting of a superposition of multiple spin-density waves, has been extensively studied in condensed matter physics since it leads to complicated noncollinear and noncoplanar magnetic orderings in materials. Noncollinear magnetic orderings give rise to electric polarization [1–4] and antisymmetric spin polarization [5,6], whereas noncoplanar magnetic orderings give rise to topological Hall and Nernst effects [7–20] and nonreciprocal transport [21,22]. These features have been ubiquitously clarified through microscopic model calculations for various lattice systems, such as noncoplanar triple- Q states on a triangular lattice [23–27] and a distorted face-centered cubic lattice [28].

Itinerant magnets are one of the typical systems for realizing multiple- Q states since effective interactions mediated by itinerant electrons often induce the multiple- Q instability. For example, the emergence of a magnetic skyrmion crystal (SkX) and vortex crystal with topologically nontrivial spin textures have been theoretically clarified as a consequence of multiple- Q states in the Kondo lattice model [29–36], even without the Dzyaloshinskii–Moriya (DM) interaction [37,38] and antisymmetric spin–orbit interaction (spin-dependent hopping). Simultaneously, such multiple- Q states have been observed in a variety of itinerant magnetic materials under centrosymmetric lattice structures, such as Gd_2PdSi_3 [16,39–47], $\text{Gd}_3\text{Ru}_4\text{Al}_{12}$ [48–51], GdRu_2Si_2 [52–56], and $\text{Y}_3\text{Co}_8\text{Sn}_4$ [57,58], as well as noncentrosymmetric lattice structures, such as MnSi [9,59–77], $\text{Fe}_{1-x}\text{Co}_x\text{Si}$ [78–82], EuPtSi [83–92], and EuNiGe_3 [93–96]. The findings of the SkX in Gd- and Eu-based compounds might be attributed to the large total angular momentum without the orbital angular momentum.

In contrast to noncentrosymmetric itinerant magnets, where the DM interaction plays an important role in stabilizing the SkX [97,98], effective multiple-spin interactions in the

form of $(\mathbf{S}_i \cdot \mathbf{S}_j)^2$ and $(\mathbf{S}_i \cdot \mathbf{S}_j)(\mathbf{S}_k \cdot \mathbf{S}_l)$ [30,35], easy-axis single-ion anisotropy in the form of $(S_i^z)^2$ [31,99], and two-spin symmetric anisotropic exchange interaction in the form of $S_i^x S_j^x$ with the directional dependence [49,100] become the origin of the SkX in centrosymmetric itinerant magnets, where $\mathbf{S}_i = (S_i^x, S_i^y, S_i^z)$ is the localized spin at site i . Meanwhile, it is usually difficult to directly identify which factors are essential in SkX-hosting materials.

In the present study, we investigate different tendencies among the above mechanisms by examining the stability of the SkX under in-plane and out-of-plane external magnetic fields. Since the symmetry of the aforementioned spin interactions differs, one can obtain different stability tendencies depending on the magnetic field directions. In order to demonstrate this, we construct two magnetic phase diagrams for an effective spin model with the two-spin symmetric anisotropic exchange interaction on a two-dimensional triangular lattice: one corresponding to the field direction lying in the xz -plane and the other corresponding to the field direction lying in the yz -plane. We show that the stability region and behavior of the triple-Q SkX are different depending on the magnetic field direction. We also show that the instability toward multiple-Q states, other than the SkX, is qualitatively different for different magnetic field directions. We discuss the differences in the phase diagrams from other mechanisms, such as multiple-spin interactions and easy-axis single-ion anisotropy. Our results would be helpful for clarifying whether the two-spin symmetric anisotropic exchange interaction plays a significant role in stabilizing the SkX in centrosymmetric itinerant magnets.

The rest of this paper is organized as follows. In Section 2, we introduce an effective spin model in centrosymmetric itinerant magnets, where the effect of the two-spin symmetric anisotropic exchange interaction is incorporated. We also outline the numerical method based on simulated annealing. In Section 3, we discuss the numerical results by focusing on the stability of the SkX in an external magnetic field. First, we show that the SkX is induced by the two-spin symmetric anisotropic exchange interaction in an out-of-plane magnetic field. Then, we discuss the stability of the SkX by rotating the field direction in the xz - and yz -planes. We compare the obtained results with those from models incorporating multiple-spin interactions and easy-axis single-ion anisotropy in Section 4. Section 5 is devoted to a summary of this paper.

2. Model and Method

We consider the following spin model on a two-dimensional triangular lattice, which is given by

$$\mathcal{H} = -2J \sum_{\nu} \left(\mathbf{S}_{Q_{\nu}} \cdot \mathbf{S}_{-Q_{\nu}} + \sum_{\alpha\beta} I_{Q_{\nu}}^{\alpha\beta} S_{Q_{\nu}}^{\alpha} S_{-Q_{\nu}}^{\beta} \right) - \sum_i \mathbf{H} \cdot \mathbf{S}_i. \quad (1)$$

where $\mathbf{S}_i = (S_i^x, S_i^y, S_i^z)$ represents the classical spin at site i with a length $|\mathbf{S}_i| = 1$; $\mathbf{S}_{Q_{\nu}} = (S_{Q_{\nu}}^x, S_{Q_{\nu}}^y, S_{Q_{\nu}}^z)$ represents the Q_{ν} component of spin moments, which is related to \mathbf{S}_i by Fourier transformation; and ν is the index for independent wave vectors in the first Brillouin zone. The first term represents the interaction defined in momentum space with the coupling constant J , which consists of the two-spin isotropic exchange interaction and symmetric anisotropic exchange interaction. $I_{Q_{\nu}}^{\alpha\beta}$ for $\alpha, \beta = x, y, z$ represents the Q_{ν} -dependent anisotropic form factor, which originates from the interplay between spin-orbit coupling and the crystalline electric field in the triangular-lattice structure, as demonstrated in Ref. [101]. The momentum-resolved bilinear exchange interaction can be mapped into the real-space one through Fourier transformation. The second term represents the Zeeman coupling term through an external magnetic field $\mathbf{H} = (H^x, H^y, H^z)$.

The spin model with the momentum-resolved interaction in Equation (1) is derived from the Kondo lattice model with classical spin by considering a situation where the Kondo coupling between itinerant electron spins and localized spins (J_K) is small compared to the bandwidth of itinerant electrons [30,101,102]. By performing perturbative analysis in terms of the Kondo coupling, one finds that the interaction in the first term in

Equation (1) corresponds to the lowest-order contribution in terms of the Kondo coupling in the expansion, i.e., $J \propto J_K^2$, which is known as the Ruderman–Kittel–Kasuya–Yosida interaction [103–105], whose magnitude is determined by the bare susceptibility of itinerant electrons depending on the band structure and Fermi level in the system. We ignore the effect of multiple-spin interactions, which appear as higher-order contributions in the expansion, by assuming that the higher-order effect is negligible, although a situation where the bare susceptibility shows distinct peak structures at Q_ν often leads to instability toward the SkX [30].

In Equation (1), we further simplify the model by taking into account the momentum-resolved interactions at particular wave vectors that provide the dominant contribution to the ground-state energy. In other words, we consider the situation where the bare susceptibility of itinerant electrons shows maxima at particular wave vectors Q_1 – Q_3 , which are often attained by the nesting of the Fermi surface. Specifically, we set $Q_1 = (Q, 0)$, $Q_2 = (-Q/2, \sqrt{3}Q/2)$, and $Q_3 = (-Q/2, -\sqrt{3}Q/2)$ with $Q = \pi/3$, where the lattice constant of the triangular lattice is taken as unity. It is noted that Q_1 , Q_2 , and Q_3 are connected by the threefold rotational symmetry of the triangular lattice. The following results are not qualitatively affected by a different choice of Q unless the ordering wave vectors lie at the Brillouin zone boundary.

For these wave vectors, $I_{Q_\nu}^{\alpha\beta}$ is given so as to satisfy the sixfold rotational symmetry as follows [101]: $-I_{Q_1}^{xx} = I_{Q_1}^{yy} = 2I_{Q_2}^{xx} = -2I_{Q_2}^{yy} = 2I_{Q_2}^{xy}/\sqrt{3} = 2I_{Q_2}^{yx}/\sqrt{3} = 2I_{Q_3}^{xx} = -2I_{Q_3}^{yy} = -2I_{Q_3}^{xy}/\sqrt{3} = -2I_{Q_3}^{yx}/\sqrt{3} \equiv I^A$. This symmetric anisotropic form factor I^A corresponds to bond-dependent interaction, such as the compass and Kitaev interactions [106–110], which become the origin of unconventional topological spin textures [111–114] and nonreciprocal magnon excitations [110]. Furthermore, this type of symmetric anisotropic exchange interaction on the triangular lattice induces the SkX even in the absence of multiple-spin interactions or easy-axis single-ion anisotropy [49,100]. We focus on the behavior of the SkX induced by I^A against the magnetic field direction in Section 3 and compare the results among different mechanisms in Section 4.

For the model in Equation (1), we construct two low-temperature magnetic phase diagrams depending on the magnetic field direction: one is the phase diagram obtained by varying the out-of-plane field H^z and the in-plane x -directional field H^x with $H^y = 0$, and the other is the phase diagram obtained by varying H^z and the y -directional field H^y with $H^x = 0$. We set the other model parameters as $J = 1$ and $I^A = 0.1$. The phase diagrams are calculated by performing simulated annealing based on the standard Metropolis algorithm with local spin updates for the system size $N = 24^2$ under periodic boundary conditions. The procedure is as follows. By taking a random spin configuration as an initial spin state, we gradually reduce the temperature from high temperatures, $T_0 = 1$ – 5 , to the final temperature, $T = 0.0001$, using the ratio $T_{n+1} = 0.999999T_n$, where T_n is the temperature at the n th-step. We perform the local spin updates in real space at each temperature up to T . At T , we further perform Monte Carlo sweeps around 10^5 – 10^6 in order to optimize the spin configuration. We independently perform the above procedure for different sets of magnetic fields. We also perform the simulations from the spin configurations obtained at low temperatures in the vicinity of the phase boundaries in order to avoid meta-stable spin configurations.

For the spin configurations obtained through simulated annealing, we calculate the spin and scalar chirality quantities to identify the magnetic phase. The order parameter corresponds to the Q_ν component of magnetic moments $m_{Q_\nu}^\eta$ with the spin component $\eta = x, y, z$, which is given by

$$m_{Q_\nu}^\eta = \frac{1}{N} \sqrt{\sum_{i,j} S_i^\alpha S_j^\alpha e^{iQ_\nu \cdot (r_i - r_j)}}, \quad (2)$$

where r_i is the position vector at site i . We also calculate $(m_{Q_v}^{xy})^2 = (m_{Q_v}^x)^2 + (m_{Q_v}^y)^2$ and $(m_{Q_v})^2 = (m_{Q_v}^x)^2 + (m_{Q_v}^y)^2 + (m_{Q_v}^z)^2$. The squared quantity $(m_{Q_v})^2$ corresponds to the susceptibility in the Q_v channel. The uniform magnetization is given by

$$M^\eta = \frac{1}{N} \sum_i S_i^\eta. \quad (3)$$

The scalar chirality is given by

$$\chi^{\text{sc}} = \frac{1}{N} \sum_\mu \sum_{R \in \mu} \chi_R^{\text{sc}}, \quad (4)$$

$$\chi_R^{\text{sc}} = S_i \cdot (S_j \times S_k), \quad (5)$$

where R denotes the position vectors at the centers of triangles and $\mu = (u, d)$ represents upward and downward triangles, respectively, in the triangular lattice. The site indices i, j, k represent the vertices on the triangle at R in counterclockwise order. The magnetic states with nonzero χ^{sc} correspond to the topologically nontrivial states since they generate an auxiliary magnetic field and act on the itinerant electrons via the spin Berry phase mechanism.

3. Results

We show the stability of the SkX and other multiple- Q states in the different magnetic field directions. In Section 3.1, we show that the SkX appears in the ground state under the out-of-plane magnetic field with the aid of the two-spin symmetric anisotropic exchange interaction. Then, we show the effect of the in-plane magnetic field on the SkX. The results under the x -directional magnetic field are shown in Section 3.2, whereas those under the y -directional magnetic field are shown in Section 3.3.

3.1. Out-of-Plane Field

First, we investigate the instability toward the SkX in the model in Equation (1) under the out-of-plane magnetic field, i.e., $H^x = H^y = 0$ and $H^z \neq 0$. In the case of $I^A = 0$, the system exhibits the single- Q conical spiral state under H^z , whose spin configuration is given by $S_i = (\sin \theta \cos Q_v \cdot r_i, \sin \theta \sin Q_v \cdot r_i, \cos \theta)$ with $\cos \theta = H^z/2$. Thus, there is no instability toward multiple- Q states in the absence of I^A .

Meanwhile, the multiple- Q states, including the SkX, appear by introducing I^A [100]. Figure 1 shows the H^z dependence of the magnetic and scalar chirality quantities at $I^A = 0.1$. For better readability, we sort $(m_{Q_v}^{xy})^2$ in Figure 1b and $(m_{Q_v}^z)^2$ in Figure 1c when the states with different Q_v are energetically degenerate. There are six phases except for the fully polarized state stabilized for $H^z \gtrsim 2.2$; the spin configuration of the fully polarized state is given by $S_i = (0, 0, 1)$. We describe the details of the obtained phases one by one below. The nonzero scalar chirality and magnetic moments in each phase are summarized in Table 1.

Phase I. This state is stabilized at zero and low fields. At zero fields, this state exhibits an anisotropic double- Q modulation; the dominant contribution is given by $(m_{Q_1}^{xy})^2$ and $(m_{Q_1}^z)^2$, and the subdominant contribution is given by $(m_{Q_2}^{xy})^2$, as shown in Figure 1b,c. Specifically, the spin configuration is represented by a superposition of the proper-screw spiral wave in the Q_1 component and the sinusoidal wave in the Q_2 component. Such a feature can be seen in the real-space spin configuration, as shown in Figure 2a, where it is noted that the dominant and subdominant components are given by $(m_{Q_3})^2$ and $(m_{Q_1})^2$, respectively. Owing to the double- Q superposition, this spin configuration is noncoplanar, and the density wave in terms of the scalar chirality occurs in the subdominant $(m_{Q_v})^2$ component, as shown in Figure 3a. On the other hand, there is no uniform scalar chirality in this state, as shown in Figure 1d.

When H^z is applied, the magnetization M^z continuously increases, as shown in Figure 1a. Accordingly, $(m_{Q_3}^{xy})^2$ becomes nonzero, as shown in Figure 1b, which indicates that Phase I is characterized by an anisotropic triple-Q state. No net scalar chirality is induced in this triple-Q spin texture, as shown in Figure 1d.

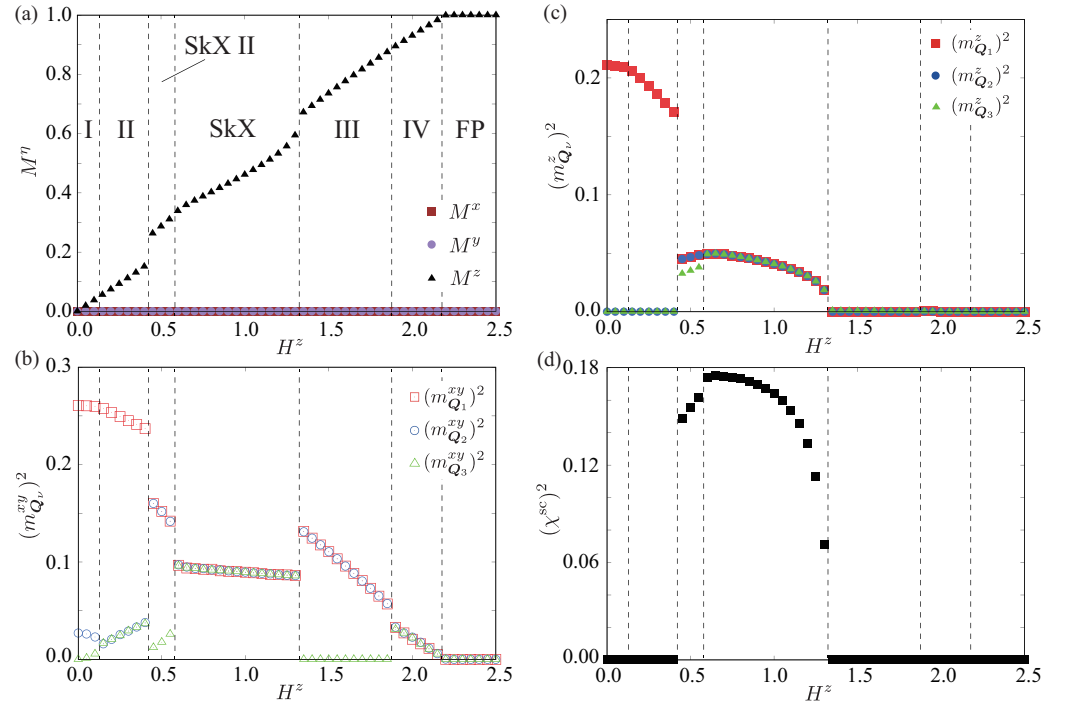


Figure 1. Out-of-plane magnetic field H^z dependence of (a) the magnetization M^η , (b) the Q_v component of the squared in-plane magnetic moment $(m_{Q_v}^{xy})^2$, (c) the Q_v component of the squared out-of-plane magnetic moment $(m_{Q_v}^z)^2$, and (d) the squared scalar chirality $(\chi^{sc})^2$ for $I^A = 0.1$ and $H^x = H^y = 0$. FP stands for the fully polarized state.

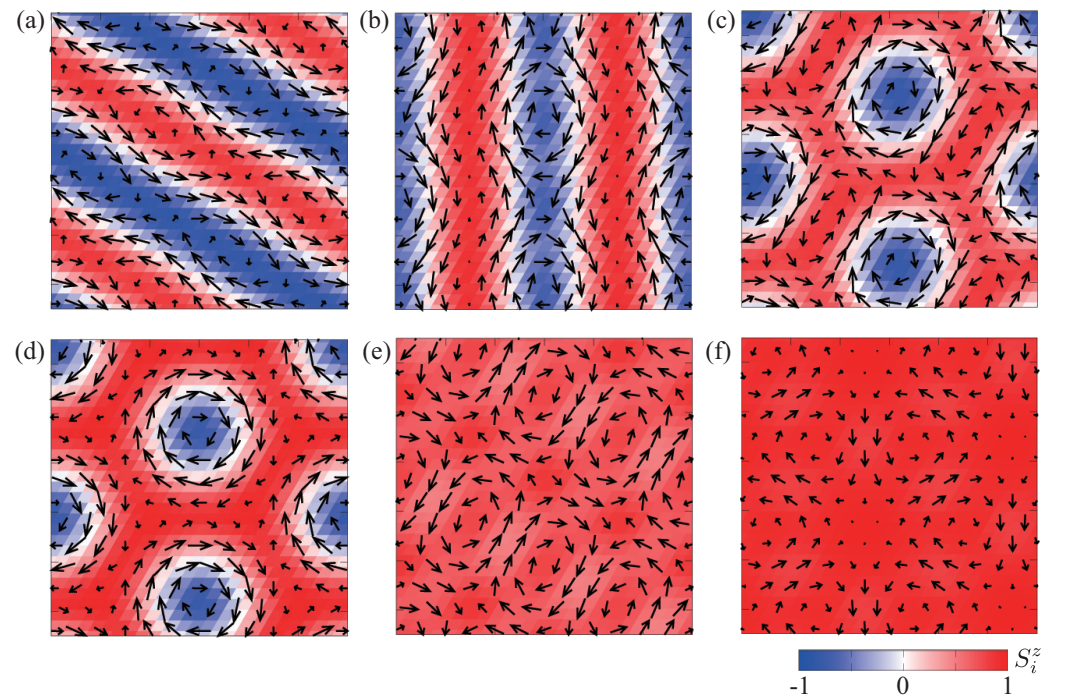


Figure 2. Real-space spin configurations of (a) Phase I at $H^z = 0$, (b) Phase II at $H^z = 0.4$, (c) SkX II at $H^z = 0.5$, (d) SkX at $H^z = 0.8$, (e) Phase III at $H^z = 1.35$, and (f) Phase IV at $H^z = 1.9$. The contour shows the z component of the spin moment, and the arrows represent the xy components.

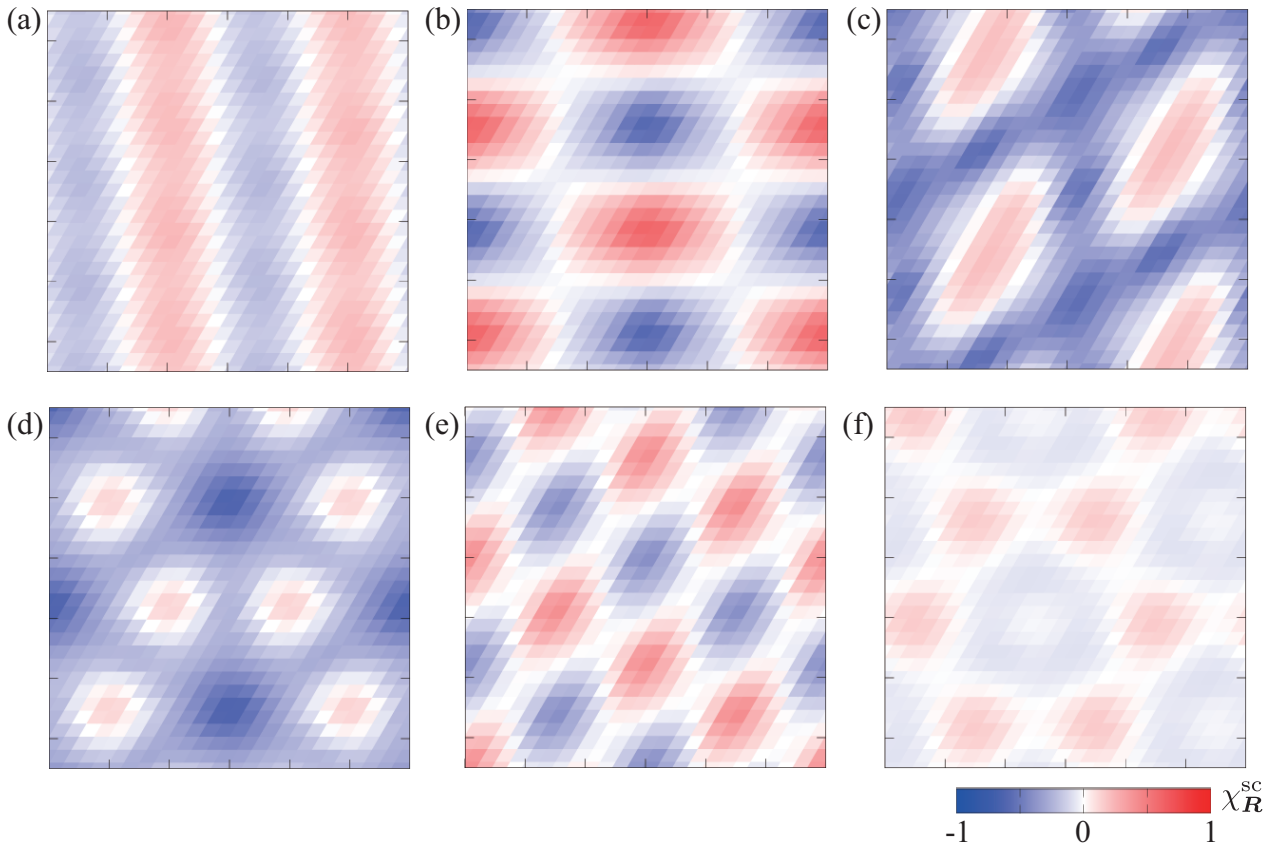


Figure 3. Real-space scalar chirality configuration corresponding to Figure 2.

Table 1. Scalar chirality χ^{sc} and Q_ν components of the magnetic moments m_{Q_ν} for $\nu = 1-3$ in each phase.

Phase	χ^{sc}	$m_{Q_1}^{xy}$	$m_{Q_1}^z$	$m_{Q_2}^{xy}$	$m_{Q_2}^z$	$m_{Q_3}^{xy}$	$m_{Q_3}^z$	Remark
Phase I	–	✓	✓	✓	–	✓	–	$(m_{Q_2}^{xy})^2 \neq (m_{Q_3}^{xy})^2$
Phase II	–	✓	✓	✓	–	✓	–	$(m_{Q_2}^{xy})^2 = (m_{Q_3}^{xy})^2$
SkX II	✓	✓	✓	✓	✓	✓	✓	$(m_{Q_1})^2 = (m_{Q_2})^2 \neq (m_{Q_3})^2$
SkX	✓	✓	✓	✓	✓	✓	✓	$(m_{Q_1})^2 = (m_{Q_2})^2 = (m_{Q_3})^2$
Phase III	–	✓	–	✓	–	–	–	$(m_{Q_1}^{xy})^2 = (m_{Q_2}^{xy})^2$
Phase IV	–	✓	–	✓	–	✓	–	$(m_{Q_1}^{xy})^2 = (m_{Q_2}^{xy})^2 = (m_{Q_3}^{xy})^2$

Phase II. This phase appears next to Phase I by increasing H^z , as shown in Figure 1a. The phase transition is of second order, where the magnetization smoothly changes, as shown in Figure 1a. The spin configuration in this phase is similar to that in Phase I, as shown in Figure 2a,b. Meanwhile, there is a small difference in $(m_{Q_\nu}^{xy})^2$ for $\nu = 2, 3$; in contrast to Phase I, the subdominant intensity in $(m_{Q_\nu}^{xy})^2$ is equal to that in $(m_{Q_3}^{xy})^2$. Reflecting this difference, the scalar chirality in real space exhibits a checkerboard-type modulation, as shown in Figure 3b, which indicates that the scalar chirality is characterized by the double-Q modulation. Similar to Phase I, this state does not exhibit a net scalar chirality.

SkX II. When the magnetic field is increased in Phase II, the SkX II appears with a jump in the magnetization, as shown in Figure 1a, which indicates a first-order phase transition.

This state is described by a superposition of the triple- Q spiral waves in the Q_1 , Q_2 , and Q_3 components. As shown in Figure 1b,c, the triple- Q superposition is anisotropic; $(m_{Q_1})^2$ is equal to $(m_{Q_2})^2$, but neither is equal to $(m_{Q_3})^2$. This feature appears in the real-space spin configuration in Figure 2c, where the shape of the skyrmion core, denoted as $S_i^z = -1$, seems elliptic rather than circular; the skyrmion core is located on the interstitial site owing to the discrete lattice structure without easy-axis single-ion anisotropy. The deviation from the circular shape of the skyrmion core is caused by the breaking of the threefold rotational symmetry, which is found in the relation $(m_{Q_1})^2 = (m_{Q_2})^2 \neq (m_{Q_3})^2$. The scalar chirality in real space is also characterized by an anisotropic triple- Q structure, as shown in Figure 3c. In contrast to Phase I and Phase II, this state exhibits a nonzero scalar chirality in Figure 1d, which signals the topologically nontrivial spin texture leading to the topological Hall effect.

SkX. With a further increase in H^z , the SkX II turns into the SkX, as shown in Figure 1a. This state is also characterized by the triple- Q spiral states, although the intensities in the triple- Q components are equivalent to each other, i.e., $(m_{Q_1}^{xy})^2 = (m_{Q_2}^{xy})^2 = (m_{Q_3}^{xy})^2$ and $(m_{Q_1}^z)^2 = (m_{Q_2}^z)^2 = (m_{Q_3}^z)^2$ in contrast to the situation in the SkX II (see Figure 1b,c). Owing to the isotropic triple- Q structure, the real-space spin configuration keeps the threefold rotational symmetry of the triangular lattice, as shown in Figure 2d. Accordingly, the scalar chirality is also distributed in a threefold-symmetric way, as shown in Figure 3d. The net scalar chirality becomes nonzero in Figure 1d.

The appearance of both the SkX and SkX II is owing to the two-spin symmetric anisotropic exchange interaction I^A . Since $I^A > 0$ ($I^A < 0$) favors the proper-screw (out-of-plane cycloidal) spiral wave, the resultant triple- Q SkX favors the Bloch (Néel) SkX. The Bloch helicity means that the spins surrounding the skyrmion core rotate in the xy -plane with a helicity of $\pm\pi/2$, whereas the Néel helicity means that the spins are radially directed in an inward or outward way with a helicity of 0 or π . Indeed, we obtain the Bloch-type helicity in both the SkX and SkX II phases for $I^A = 0.1 > 0$, as shown in Figure 2c,d. It is noted that the introduction of I^A lifts the degeneracy with the anti-type SkX with the opposite sign of the scalar chirality. A similar situation also occurs in the square SkX in the tetragonal lattice system [115].

Phase III. This phase appears upon increasing H^z in the SkX with a jump in the magnetization, as shown in Figure 1a. The phase transition between Phase III and SkX is of first order. The spin configuration in this state is characterized by the sinusoidal waves in two out of three $(m_{Q_\nu}^{xy})^2$, as shown in Figure 1b, which means the appearance of the double- Q fan state. On the other hand, there are no z -spin modulations in the Q_ν component, as shown in Figure 1c. The in-plane double- Q spin texture leads to the periodic alignment of the vortex and anti-vortex, as shown by the real-space spin configuration in Figure 2e. The distribution of the scalar chirality is described by a superposition of the $Q_1 - Q_2$ and Q_3 components when the magnetic modulations are represented by the Q_1 and Q_2 components, as shown in Figure 3e. Owing to the equivalence of the vortex and anti-vortex, the net scalar chirality becomes zero in the whole system, as shown in Figure 1d. One finds that the scalar chirality shows a jump from the finite values to zero in the transition from the SkX, as shown in Figure 1d.

Phase IV. This phase is stabilized in the high-field region close to the saturation field, as shown in Figure 1a. As shown in Figure 1b,c, the spin configuration in this state is described by an in-plane triple- Q fan structure with nonzero $(m_{Q_1}^{xy})^2 = (m_{Q_2}^{xy})^2 = (m_{Q_3}^{xy})^2$ but without $(m_{Q_\nu}^z)^2$. The real-space spin and scalar chirality configurations are shown in Figures 2f and 3f, respectively, where the threefold symmetric distributions are seen in both configurations. In the real-space picture, one finds two types of vortices: one is the vortex with a winding number of -2 , whereas the other is the vortex with a winding number of $+1$. Since the number of the vortex with the winding number of $+1$ is twice that of the one with the winding number of -2 , the net scalar chirality becomes zero in the whole system. A similar spin texture is also found in the frustrated triangular-lattice magnets [116,117]. This phase continuously turns into a fully polarized state with the increase in the magnetic field.

3.2. In-Plane Field along the x -Direction

We investigated the effect of the in-plane magnetic field on the SkX and other multiple- Q states obtained in Section 3.1. In this section, we examine the effect of the x -directional magnetic field H^x while keeping $H^y = 0$. Figure 4 shows the low-temperature phase diagram when H^x and H^z are varied. The contours in Figure 4a–d represent $(\chi^{\text{sc}})^2$ in Figure 4a, $(m_{Q_1})^2$ in Figure 4b, $(m_{Q_2})^2$ in Figure 4c, and $(m_{Q_3})^2$ in Figure 4d.

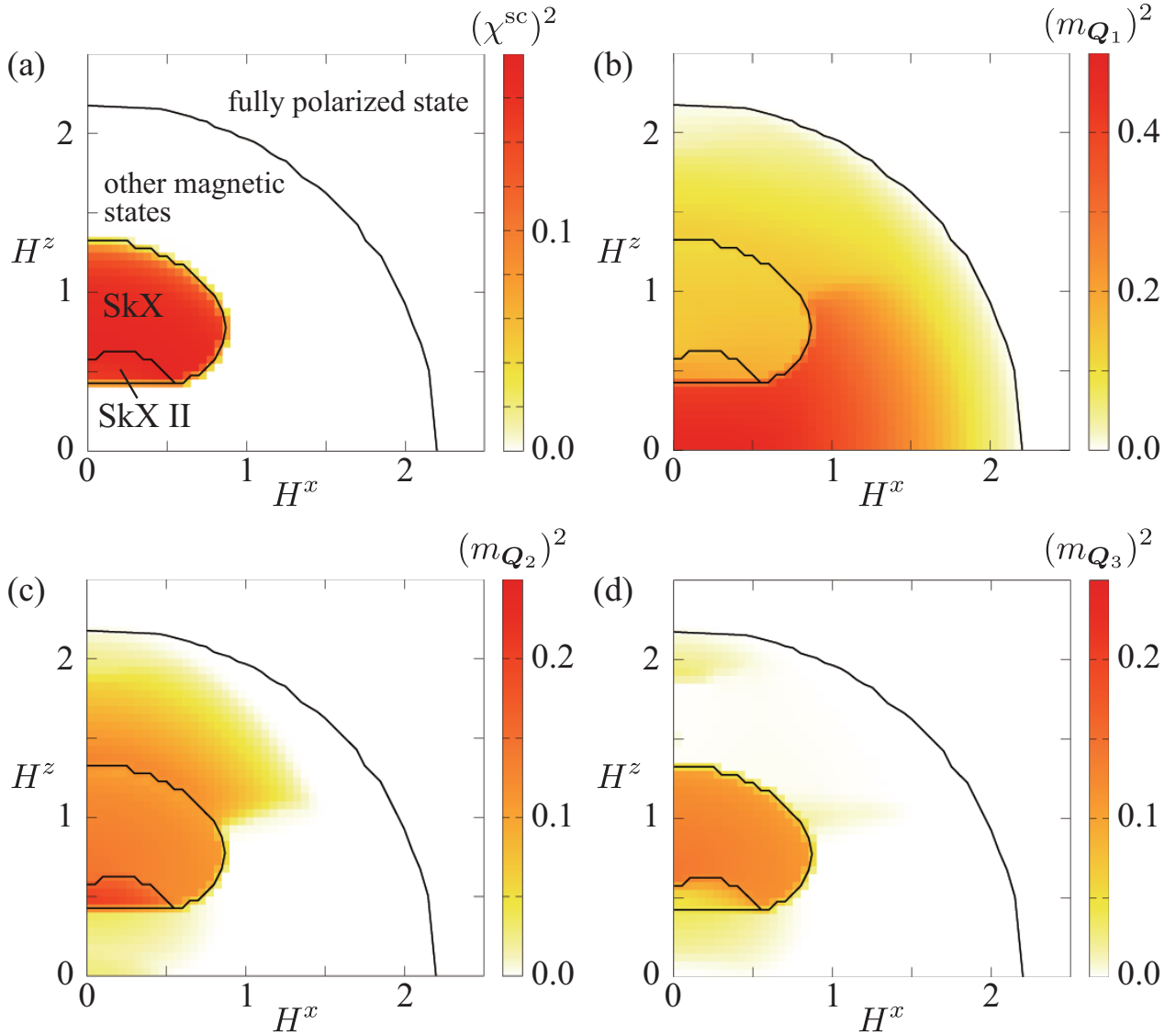


Figure 4. Low-temperature phase diagram under the magnetic field in the xz -plane. The contour shows (a) $(\chi^{\text{sc}})^2$, (b) $(m_{Q_1})^2$, (c) $(m_{Q_2})^2$, and (d) $(m_{Q_3})^2$.

Since $(\chi^{\text{sc}})^2$ becomes nonzero only for the SkX and SkX II, this quantity signals the appearance of the skyrmion spin texture. As shown in Figure 4a, both SkX phases remain stable when the magnetic field is tilted from the out-of-plane direction to the in-plane x -direction up to around 54° measured from the z -axis. Then, both SkX phases vanish when H^x is further increased, which indicates that I^A does not favor the SkX in an in-plane magnetic field along the x -direction. This is consistent with the results that the easy-plane single-ion anisotropy in the form of $A(S_z^2)^2$ for $A > 0$ is required in order to stabilize the SkX in the in-plane magnetic field [118].

Since the magnetic field is tilted from the z -direction, the threefold rotational symmetry of the SkX is broken; the Q_1 component is no longer equivalent to the Q_2 and Q_3

components. Accordingly, the skyrmion core is elongated along the y -direction, as shown by the real-space spin configuration in Figure 5a. The scalar chirality distribution is also modulated so as to break the threefold rotational symmetry, although such a change is small, as shown in Figure 5b. Indeed, $(\chi^{\text{sc}})^2$ takes similar values in the entire region where the SkX and SkX II phases appear, as shown in Figure 4a. Meanwhile, the skyrmion size under the in-plane field is almost the same as that under the out-of-plane field since the present SkX consists of a superposition of spin-density waves at the same ordering wave vectors.

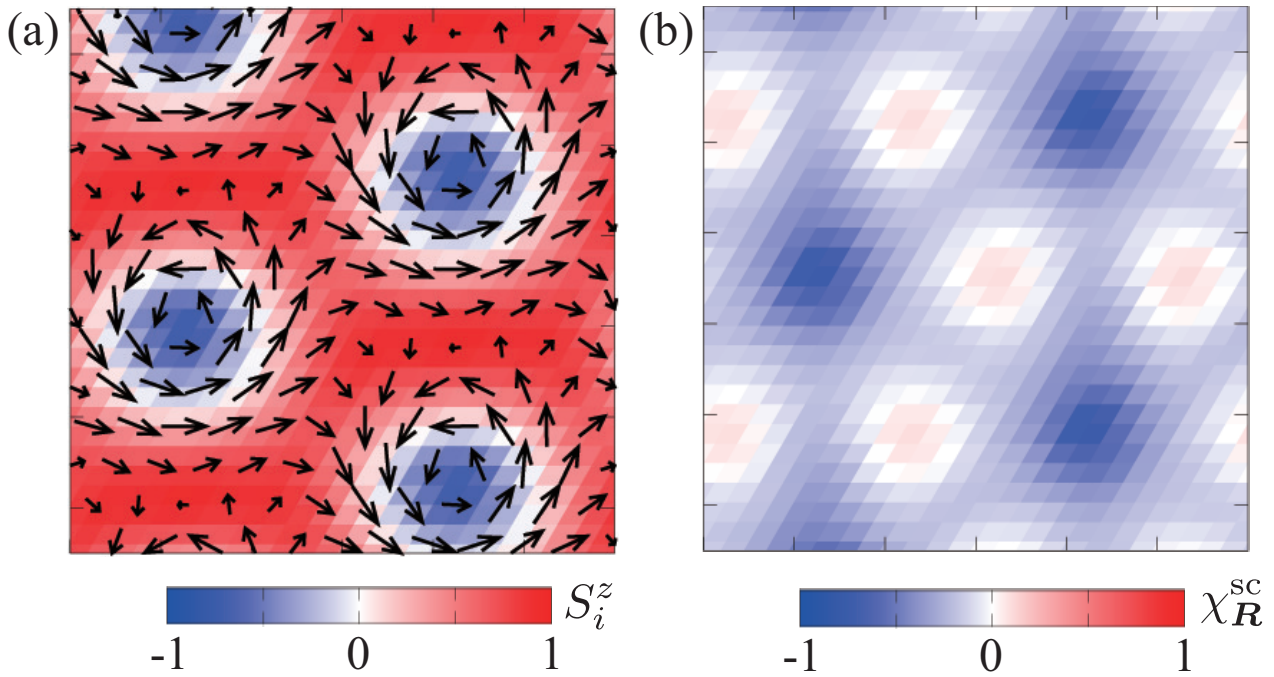


Figure 5. (a) Real-space spin configurations of the SkX at $H^x = 0.75$ and $H^z = 0.8$. (b) Real-space scalar chirality configurations corresponding to (a).

We discuss the effect of the x -directional magnetic field on the other phases by examining the data at $H^x = 0.4$ in Figure 6a–d and $H^x = 0.8$ in Figure 6e–h. In the low-field region for $H^z \lesssim 0.4$ at $H^x = 0.4$, the behavior of $(m_{Q_v}^{xy})^2$ is similar to that at $H^x = 0$, as shown in Figures 1b and 6b. Meanwhile, $(m_{Q_2}^z)^2$ and $(m_{Q_3}^z)^2$ become nonzero for $0.1 \lesssim H^z \lesssim 0.4$ in Figure 6c, which is different from the result in Figure 1c. Thus, we denote this phase as Phase II' instead of Phase II. By increasing H^x , $(m_{Q_2}^z)^2$ and $(m_{Q_3}^z)^2$ vanish while keeping nonzero $(m_{Q_1}^z)^2$ for $0 \lesssim H^z \lesssim 0.6$, as shown in Figure 6f,g, which indicates that the magnetic structure is characterized by the single- Q spiral state; we denote it as Phase I'. The choice of the spiral waves in the Q_1 component is attributed to the energy gain by both I^A and H^x since the spiral plane lies on the yz -plane for the Q_1 component.

In the high-field region for $1.3 \lesssim H^z \lesssim 2.2$ at $H^x = 0.4$, the magnitudes of the triple- Q ordering wave vectors become nonzero with different intensities in both the xy and z components, as shown in Figure 6b,c. We denote this phase as Phase III'. Such a feature holds for larger H^x , as shown in the case of $H^x = 0.8$ in Figure 6f,g. This anisotropic triple- Q phase is replaced with the single- Q state stabilized in the low-field region by further increasing H^x , as shown in Figure 4b–d. The net scalar chirality remains zero in the regions of Phase I', Phase II', and Phase III', as shown in Figure 6d,h.

3.3. In-Plane Field along the y -Direction

Next, we discuss the results obtained by rotating the magnetic field on the yz -plane, i.e., $H^x = 0$. Figure 7a–d show the phase diagram in the plane of H^y and H^z . Similar to

the results in Figure 4, we show the contours of $(\chi^{\text{sc}})^2$ in Figure 7a, $(m_{Q_1})^2$ in Figure 7b, $(m_{Q_2})^2$ in Figure 7c, and $(m_{Q_3})^2$ in Figure 7d.

The SkX remains stable up to $H^y \sim 0.9$, as shown in Figure 7a. The stability region of the SkX under H^y is similar to that under H^x , although one can observe a slight difference between them; the SkX region for the former case is wider than that for the latter. The real-space spin and scalar chirality configurations in the presence of H^y are shown in Figures 8a and 8b, respectively. Owing to the y -directional magnetic field, the spins tend to align the positive y -direction, which breaks the threefold rotational symmetry. In contrast to the result under H^x , the SkX and SkX II are not distinguished from each other when H^y is introduced, which means that they smoothly merge into a single phase, as shown in Figure 9b,c.

In the low- and high-field regions, the instabilities toward the magnetic states are qualitatively different from those in Section 3.2. In the low-field region, the dominant intensity of $(m_{Q_\nu})^2$ is found in the Q_2 (or Q_3) component in order to gain the Zeeman energy with H^y , as shown in Figure 9b,c,f,g. We denote this phase as Phase I''. In addition, the magnetic state with dominant double-Q intensities $(m_{Q_2})^2 = (m_{Q_3})^2$ appears in the high-field region, where we denote it as Phase III'', as shown in Figure 9b,c,f,g. It is noted that $(m_{Q_1})^2$ is slightly induced in this state. This phase remains stable with the increase in H^y ; the double-Q feature can be seen in the vicinity of $H^z = 0$ and $H^y = 2$, as shown in Figure 7c,d. Thus, one can find that the importance of I^A can be tested by examining the magnetic phases against H^x and H^y for $H^z = 0$. When I^A plays an important role, the magnetic phase corresponds to the single-Q spiral state for $H^x \neq 0$, whereas it corresponds to the triple-Q state with strong double-Q spin modulations for $H^y \neq 0$.

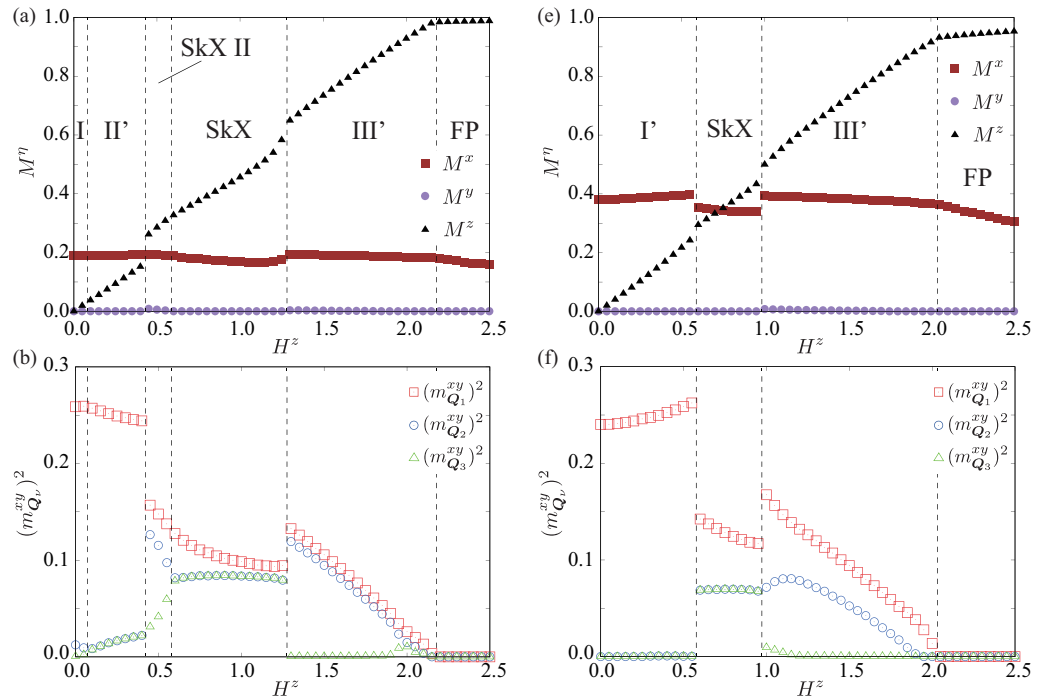


Figure 6. Cont.

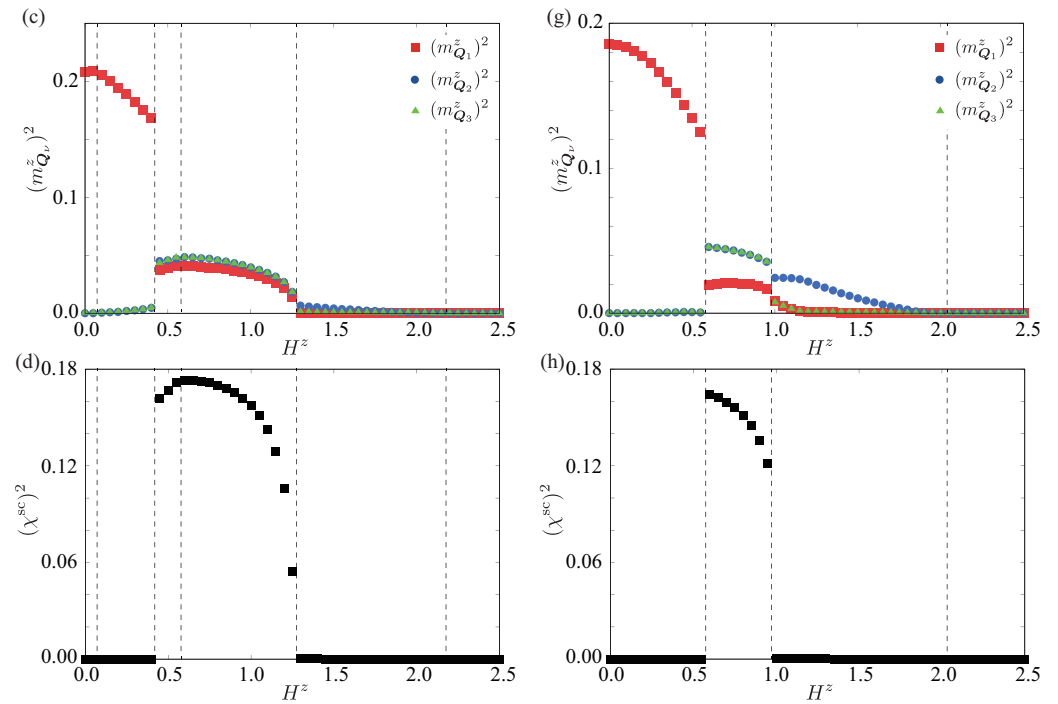


Figure 6. H^z dependence of (a,e) M^y , (b,f) $(m_{Q_v}^{xy})^2$, (c,g) $(m_{Q_v}^z)^2$, and (d,h) $(\chi^{sc})^2$ for (a–d) $H^x = 0.4$ and (e–h) $H^x = 0.8$. The vertical dashed lines represent the phase boundaries between different magnetic phases.

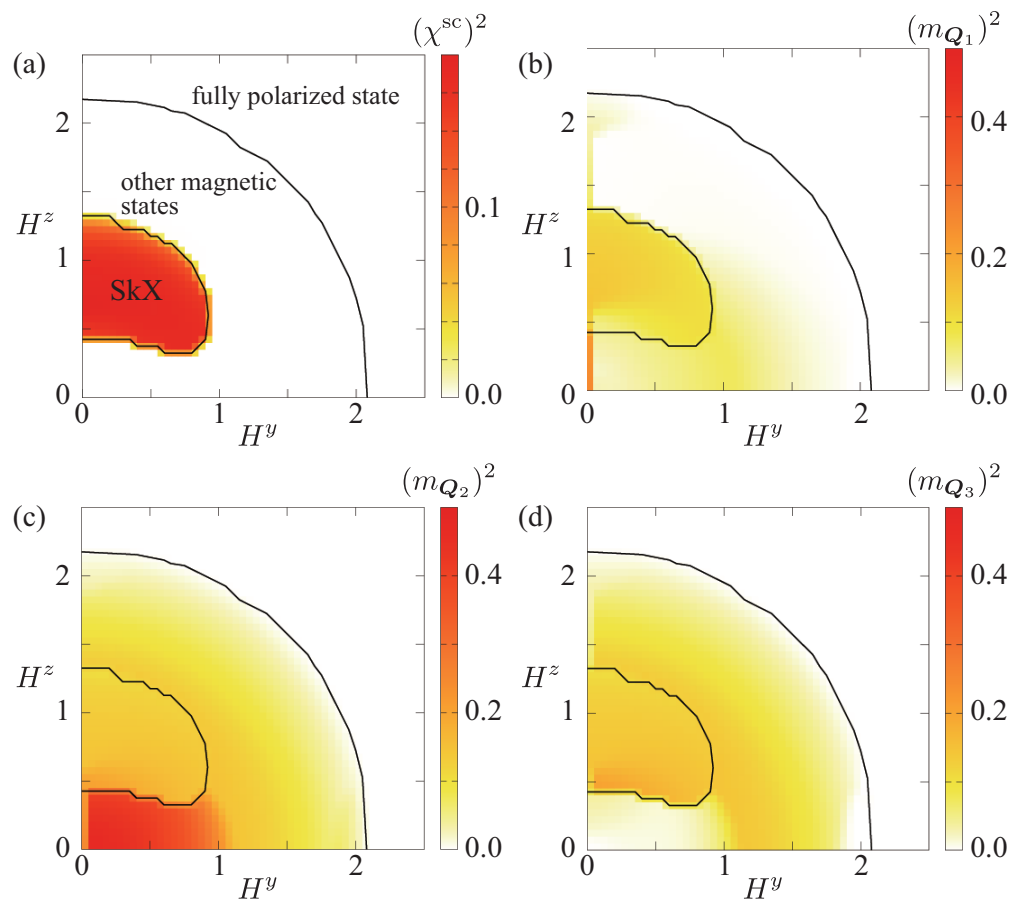


Figure 7. Low-temperature phase diagram under the magnetic field in the yz -plane. The contour shows (a) $(\chi^{sc})^2$, (b) $(m_{Q_1})^2$, (c) $(m_{Q_2})^2$, and (d) $(m_{Q_3})^2$.

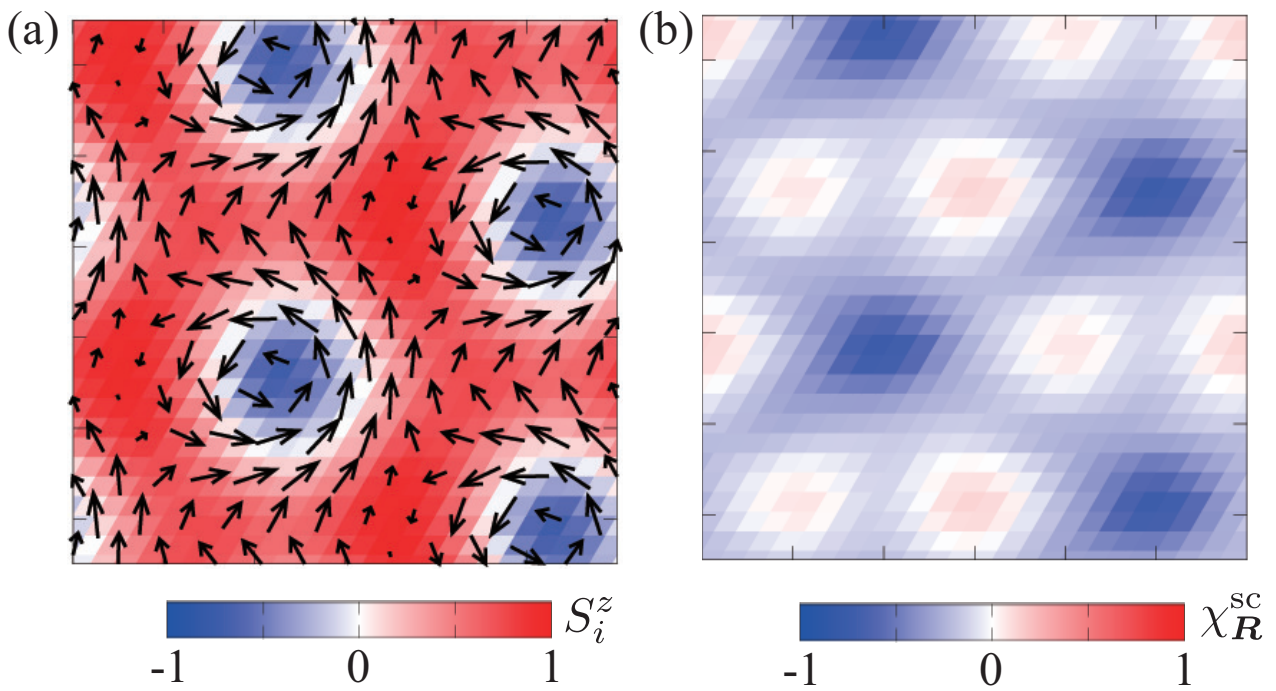


Figure 8. (a) Real-space spin configurations of the SkX at $H^y = 0.8$ and $H^z = 0.8$. (b) Real-space scalar chirality configurations corresponding to (a).

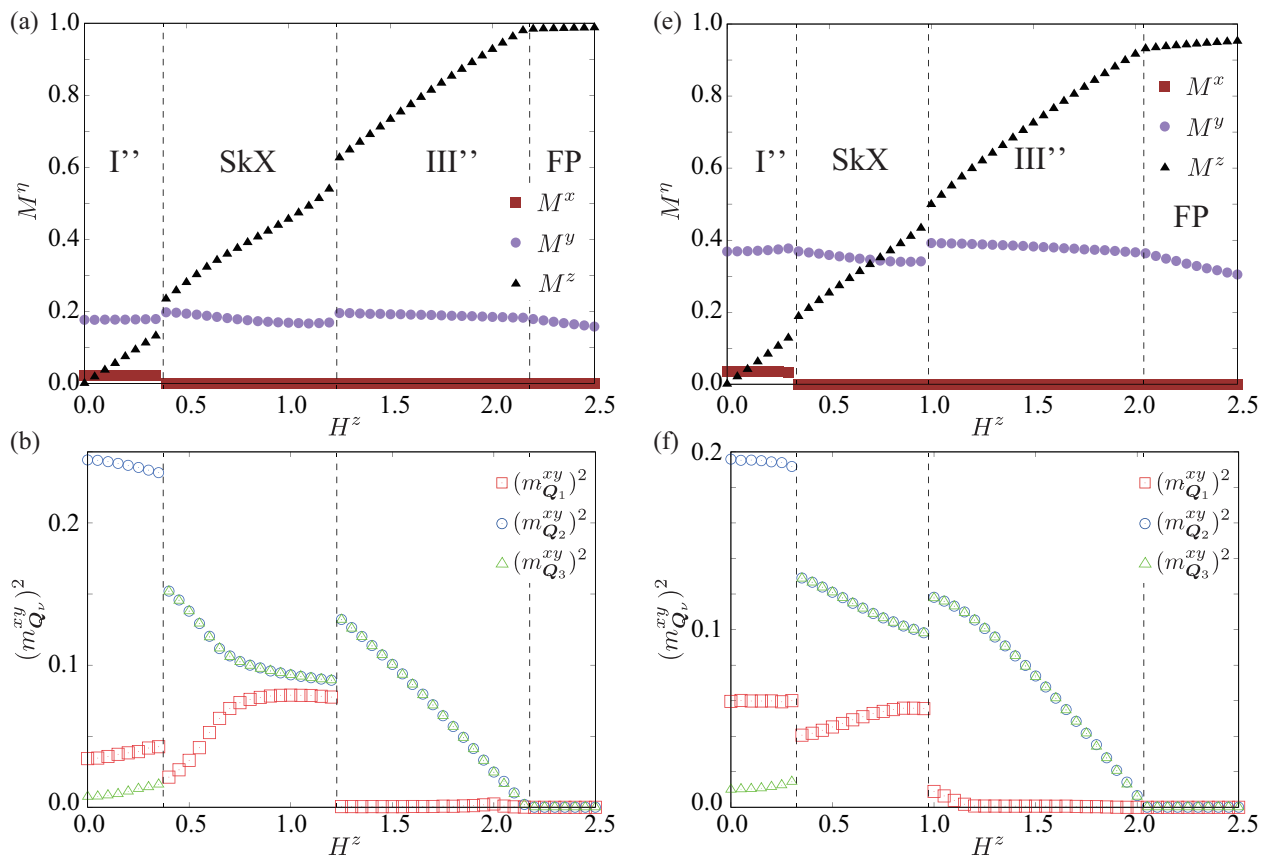


Figure 9. Cont.

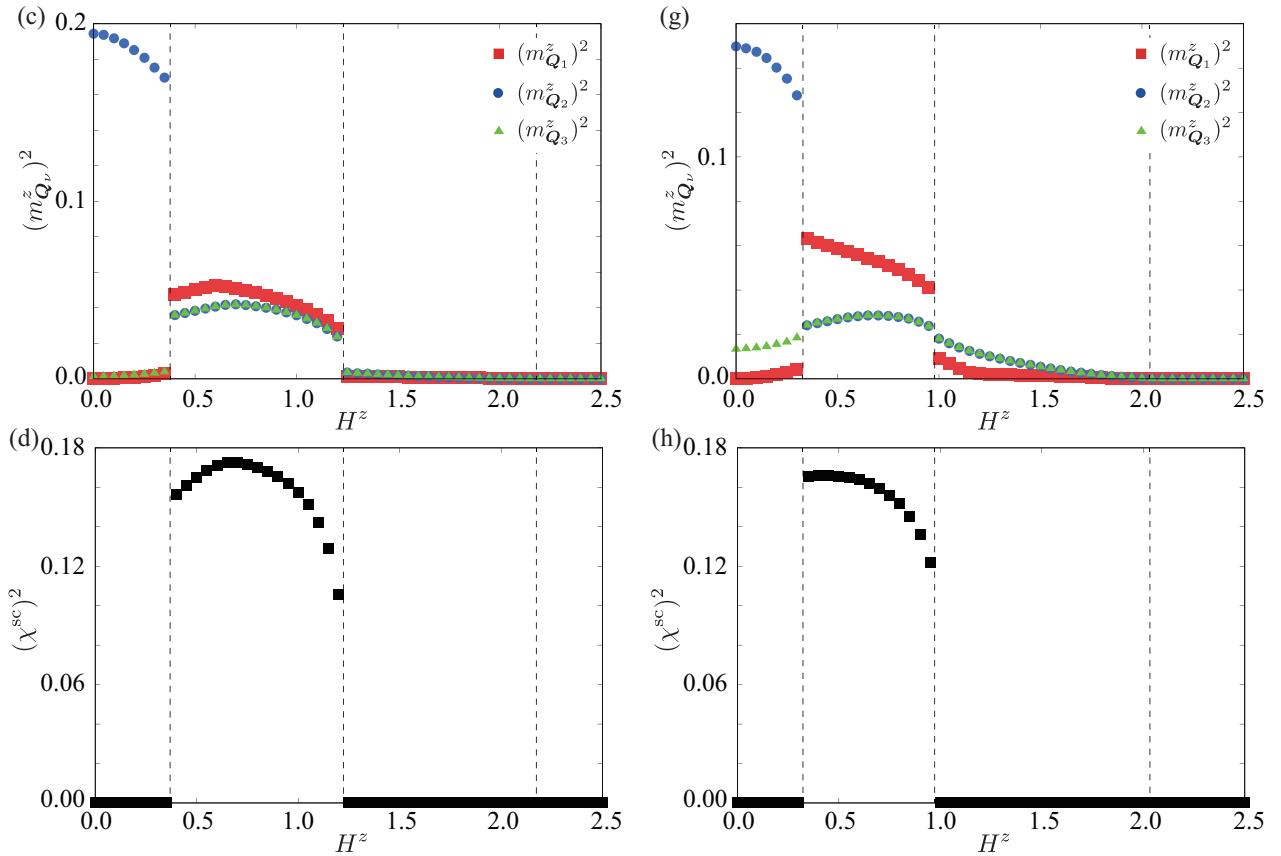


Figure 9. H^z dependence of (a,e) M^y , (b,f) $(m_{Q_v}^{xy})^2$, (c,g) $(m_{Q_v}^z)^2$, and (d,h) $(\chi^{sc})^2$ for (a–d) $H^y = 0.4$ and (e–h) $H^y = 0.8$. The vertical dashed lines represent the phase boundaries between different magnetic phases.

4. Comparison with Other Mechanisms

Finally, let us briefly compare the present results with other results obtained under different interactions and magnetic anisotropy. In the present model, we consider the situation where the SkX is induced by the two-spin symmetric anisotropic exchange interaction I^A . Meanwhile, there are other mechanisms to induce the SkX in centrosymmetric itinerant magnets, such as the positive biquadratic interaction in the form of $(S_q \cdot S_{-q})^2$ [30] and the easy-axis single-ion anisotropy in the form of $-A(S_i^z)^2$ [31,100]. Although the phase diagrams under the out-of-plane magnetic field are similar to each other, those under the in-plane field are expected to be different, which is easily understood from the symmetry aspect.

In the case of the positive biquadratic interaction, the effect of the x -directional field is the same as that of the y -directional field since this isotropic interaction is invariant under spin rotation. Similarly, the easy-axis single-ion anisotropy also does not bring about a difference in terms of H^x and H^y owing to the spin rotational symmetry around the z -axis. Thus, the mechanism based on the two-spin symmetric anisotropic exchange interaction can be distinguished from the other two mechanisms by investigating the magnetic states under the in-plane magnetic fields along the two directions.

5. Summary

We have numerically investigated the effect of the in-plane magnetic field on the SkX in centrosymmetric itinerant magnets with the two-spin symmetric anisotropic exchange interaction. By performing simulated annealing for the effective spin model with the momentum-resolved interaction on the triangular lattice and constructing two magnetic phase diagrams in the in-plane x - and y -directional magnetic fields, we show the similarity and difference of the SkX stability according to the field direction. Furthermore, we show that the different instabilities toward the magnetic phases are caused by the different in-plane field directions, which enable us to distinguish the microscopic mechanism of the SkX induced by the two-spin symmetric anisotropic exchange interaction from the others by the multiple-spin interaction and single-ion anisotropy. One of the candidate materials is the breathing kagome compound $\text{Gd}_3\text{Ru}_4\text{Al}_{12}$ [50,51,119–121], where the SkX has been identified in experiments [48], and its emergence has been accounted for by the two-spin symmetric anisotropic exchange interaction [49].

Funding: This research was supported by the JSPS KAKENHI Grants, Numbers JP21H01037, JP22H04468, JP22H00101, JP22H01183, JP23H04869, and JP23K03288, and by JST PRESTO (JPMJPR20L8) and JST CREST (JPMJCR23O4). Parts of the numerical calculations were performed in the supercomputing systems at ISSP, the University of Tokyo.

Informed Consent Statement: Not applicable.

Data Availability Statement: The data presented in this study are available on request from the corresponding author.

Conflicts of Interest: The author declares no conflict of interest.

References

1. Katsura, H.; Nagaosa, N.; Balatsky, A.V. Spin Current and Magnetoelectric Effect in Noncollinear Magnets. *Phys. Rev. Lett.* **2005**, *95*, 057205. [[CrossRef](#)]
2. Mostovoy, M. Ferroelectricity in Spiral Magnets. *Phys. Rev. Lett.* **2006**, *96*, 067601. [[CrossRef](#)] [[PubMed](#)]
3. Cheong, S.W.; Mostovoy, M. Multiferroics: A magnetic twist for ferroelectricity. *Nat. Mater.* **2007**, *6*, 13–20. [[CrossRef](#)] [[PubMed](#)]
4. Tokura, Y.; Seki, S.; Nagaosa, N. Multiferroics of spin origin. *Rep. Prog. Phys.* **2014**, *77*, 076501. [[CrossRef](#)] [[PubMed](#)]
5. Zhang, J.; Levy, P.M.; Zhang, S.; Antropov, V. Identification of Transverse Spin Currents in Noncollinear Magnetic Structures. *Phys. Rev. Lett.* **2004**, *93*, 256602. [[CrossRef](#)] [[PubMed](#)]
6. Hayami, S.; Yanagi, Y.; Kusunose, H. Spontaneous antisymmetric spin splitting in noncollinear antiferromagnets without spin-orbit coupling. *Phys. Rev. B* **2020**, *101*, 220403. [[CrossRef](#)]
7. Ohgushi, K.; Murakami, S.; Nagaosa, N. Spin anisotropy and quantum Hall effect in the Kagomé Lattice: Chiral Spin State Based A Ferromagnet. *Phys. Rev. B* **2000**, *62*, R6065–R6068. [[CrossRef](#)]
8. Tatara, G.; Kawamura, H. Chirality-driven anomalous Hall effect in weak coupling regime. *J. Phys. Soc. Jpn.* **2002**, *71*, 2613–2616. [[CrossRef](#)]
9. Neubauer, A.; Pfleiderer, C.; Binz, B.; Rosch, A.; Ritz, R.; Niklowitz, P.G.; Böni, P. Topological Hall Effect in the A Phase of MnSi. *Phys. Rev. Lett.* **2009**, *102*, 186602. [[CrossRef](#)]
10. Kanazawa, N.; Onose, Y.; Arima, T.; Okuyama, D.; Ohoyama, K.; Wakimoto, S.; Kakurai, K.; Ishiwata, S.; Tokura, Y. Large Topological Hall Effect in a Short-Period Helimagnet MnGe. *Phys. Rev. Lett.* **2011**, *106*, 156603. [[CrossRef](#)]
11. Shiomi, Y.; Kanazawa, N.; Shibata, K.; Onose, Y.; Tokura, Y. Topological Nernst effect in a three-dimensional skyrmion-lattice phase. *Phys. Rev. B* **2013**, *88*, 064409. [[CrossRef](#)]
12. Hamamoto, K.; Ezawa, M.; Nagaosa, N. Quantized topological Hall effect in skyrmion crystal. *Phys. Rev. B* **2015**, *92*, 115417. [[CrossRef](#)]
13. Göbel, B.; Mook, A.; Henk, J.; Mertig, I. Unconventional topological Hall effect in skyrmion crystals caused by the topology of the lattice. *Phys. Rev. B* **2017**, *95*, 094413. [[CrossRef](#)]
14. Leroux, M.; Stolt, M.J.; Jin, S.; Pete, D.V.; Reichhardt, C.; Maiorov, B. Skyrmion lattice topological Hall effect near room temperature. *Sci. Rep.* **2018**, *8*, 15510. [[CrossRef](#)]

15. Nakazawa, K.; Bibes, M.; Kohno, H. Topological Hall effect from strong to weak coupling. *J. Phys. Soc. Jpn.* **2018**, *87*, 033705. [[CrossRef](#)]
16. Kurumaji, T.; Nakajima, T.; Hirschberger, M.; Kikkawa, A.; Yamasaki, Y.; Sagayama, H.; Nakao, H.; Taguchi, Y.; Arima, T.H.; Tokura, Y. Skyrmion lattice with a giant topological Hall effect in a frustrated triangular-lattice magnet. *Science* **2019**, *365*, 914–918. [[CrossRef](#)] [[PubMed](#)]
17. Matsui, A.; Nomoto, T.; Arita, R. Skyrmion-size dependence of the topological Hall effect: A real-space calculation. *Phys. Rev. B* **2021**, *104*, 174432. [[CrossRef](#)]
18. Park, H.; Heinonen, O.; Martin, I. First-principles study of magnetic states and the anomalous Hall conductivity of $M\text{Nb}_3\text{S}_6$ ($M = \text{Co}, \text{Fe}, \text{Mn}, \text{and Ni}$). *Phys. Rev. Mater.* **2022**, *6*, 024201. [[CrossRef](#)]
19. Oike, H.; Ebino, T.; Koretsune, T.; Kikkawa, A.; Hirschberger, M.; Taguchi, Y.; Tokura, Y.; Kagawa, F. Topological Nernst effect emerging from real-space gauge field and thermal fluctuations in a magnetic skyrmion lattice. *Phys. Rev. B* **2022**, *106*, 214425. [[CrossRef](#)]
20. Takagi, H.; Takagi, R.; Minami, S.; Nomoto, T.; Ohishi, K.; Suzuki, M.T.; Yanagi, Y.; Hirayama, M.; Khanh, N.; Karube, K.; et al. Spontaneous topological Hall effect induced by non-coplanar antiferromagnetic order in intercalated van der Waals materials. *Nat. Phys.* **2023**, *19*, 961. [[CrossRef](#)]
21. Cheon, S.; Lee, H.W.; Cheong, S.W. Nonreciprocal spin waves in a chiral antiferromagnet without the Dzyaloshinskii-Moriya interaction. *Phys. Rev. B* **2018**, *98*, 184405. [[CrossRef](#)]
22. Hayami, S.; Yatsushiro, M. Nonlinear nonreciprocal transport in antiferromagnets free from spin-orbit coupling. *Phys. Rev. B* **2022**, *106*, 014420. [[CrossRef](#)]
23. Martin, I.; Batista, C.D. Itinerant Electron-Driven Chiral Magnetic Ordering and Spontaneous Quantum Hall Effect in Triangular Lattice Models. *Phys. Rev. Lett.* **2008**, *101*, 156402. [[CrossRef](#)]
24. Akagi, Y.; Motome, Y. Spin Chirality Ordering and Anomalous Hall Effect in the Ferromagnetic Kondo Lattice Model on a Triangular Lattice. *J. Phys. Soc. Jpn.* **2010**, *79*, 083711. [[CrossRef](#)]
25. Kumar, S.; van den Brink, J. Frustration-Induced Insulating Chiral Spin State in Itinerant Triangular-Lattice Magnets. *Phys. Rev. Lett.* **2010**, *105*, 216405. [[CrossRef](#)] [[PubMed](#)]
26. Hayami, S.; Motome, Y. Multiple- Q instability by ($d-2$)-dimensional connections of Fermi surfaces. *Phys. Rev. B* **2014**, *90*, 060402. [[CrossRef](#)]
27. Ido, K.; Misawa, T. Many-body Chern insulator in the Kondo lattice model on a triangular lattice. *arXiv* **2023**, arXiv:2310.07094.
28. Shindou, R.; Nagaosa, N. Orbital Ferromagnetism and Anomalous Hall Effect in Antiferromagnets on the Distorted fcc Lattice. *Phys. Rev. Lett.* **2001**, *87*, 116801. [[CrossRef](#)]
29. Ozawa, R.; Hayami, S.; Motome, Y. Zero-Field Skyrmions with a High Topological Number in Itinerant Magnets. *Phys. Rev. Lett.* **2017**, *118*, 147205. [[CrossRef](#)]
30. Hayami, S.; Ozawa, R.; Motome, Y. Effective bilinear-biquadratic model for noncoplanar ordering in itinerant magnets. *Phys. Rev. B* **2017**, *95*, 224424. [[CrossRef](#)]
31. Wang, Z.; Su, Y.; Lin, S.Z.; Batista, C.D. Skyrmion Crystal from RKKY Interaction Mediated by 2D Electron Gas. *Phys. Rev. Lett.* **2020**, *124*, 207201. [[CrossRef](#)] [[PubMed](#)]
32. Hayami, S.; Okubo, T.; Motome, Y. Phase shift in skyrmion crystals. *Nat. Commun.* **2021**, *12*, 6927. [[CrossRef](#)] [[PubMed](#)]
33. Eto, R.; Pohle, R.; Mochizuki, M. Low-Energy Excitations of Skyrmion Crystals in a Centrosymmetric Kondo-Lattice Magnet: Decoupled Spin-Charge Excitations and Nonreciprocity. *Phys. Rev. Lett.* **2022**, *129*, 017201. [[CrossRef](#)]
34. Wang, Z.; Batista, C.D. Skyrmion crystals in the triangular Kondo lattice model. *SciPost Phys.* **2023**, *15*, 161. [[CrossRef](#)]
35. Sharma, V.; Wang, Z.; Batista, C.D. Machine learning assisted derivation of minimal low-energy models for metallic magnets. *Npj Comput. Mater.* **2023**, *9*, 192. [[CrossRef](#)]
36. Miyazaki, Y. Equivariant neural networks for spin dynamics simulations of itinerant magnets. *Mach. Learn. Sci. Technol.* **2023**, *4*, 045006. [[CrossRef](#)]
37. Dzyaloshinsky, I. A thermodynamic theory of “weak” ferromagnetism of antiferromagnetics. *J. Phys. Chem. Solids* **1958**, *4*, 241–255. [[CrossRef](#)]
38. Moriya, T. Anisotropic superexchange interaction and weak ferromagnetism. *Phys. Rev.* **1960**, *120*, 91. [[CrossRef](#)]
39. Hirschberger, M.; Spitz, L.; Nomoto, T.; Kurumaji, T.; Gao, S.; Masell, J.; Nakajima, T.; Kikkawa, A.; Yamasaki, Y.; Sagayama, H.; et al. Topological Nernst Effect of the Two-Dimensional Skyrmion Lattice. *Phys. Rev. Lett.* **2020**, *125*, 076602. [[CrossRef](#)]
40. Sampathkumar, E.V. A report of (topological) Hall anomaly two decades ago in Gd_2PdSi_3 , and its relevance to the history of the field of Topological Hall Effect due to magnetic skyrmions. *arXiv* **2019**, arXiv:1910.09194.
41. Kumar, R.; Iyer, K.K.; Paulose, P.L.; Sampathkumar, E.V. Magnetic and transport anomalies in $R_2\text{RhSi}_3$ ($R = \text{Gd}, \text{Tb}, \text{and Dy}$) resembling those of the exotic magnetic material Gd_2PdSi_3 . *Phys. Rev. B* **2020**, *101*, 144440. [[CrossRef](#)]

42. Zhang, H.; Huang, Q.; Hao, L.; Yang, J.; Noordhoek, K.; Pandey, S.; Zhou, H.; Liu, J. Anomalous magnetoresistance in centrosymmetric skyrmion-lattice magnet Gd_2PdSi_3 . *New J. Phys.* **2020**, *22*, 083056. [[CrossRef](#)]
43. Spachmann, S.; Elghandour, A.; Frontzek, M.; Löser, W.; Klingeler, R. Magnetoelastic coupling and phases in the skyrmion lattice magnet Gd_2PdSi_3 discovered by high-resolution dilatometry. *Phys. Rev. B* **2021**, *103*, 184424. [[CrossRef](#)]
44. Paddison, J.A.M.; Rai, B.K.; May, A.F.; Calder, S.; Stone, M.B.; Frontzek, M.D.; Christianson, A.D. Magnetic Interactions of the Centrosymmetric Skyrmion Material Gd_2PdSi_3 . *Phys. Rev. Lett.* **2022**, *129*, 137202. [[CrossRef](#)] [[PubMed](#)]
45. Bouaziz, J.; Mendive-Tapia, E.; Blügel, S.; Staunton, J.B. Fermi-Surface Origin of Skyrmion Lattices in Centrosymmetric Rare-Earth Intermetallics. *Phys. Rev. Lett.* **2022**, *128*, 157206. [[CrossRef](#)] [[PubMed](#)]
46. Ju, J.; Saito, H.; Kurumaji, T.; Hirschberger, M.; Kikkawa, A.; Taguchi, Y.; Arima, T.H.; Tokura, Y.; Nakajima, T. Polarized neutron scattering study of the centrosymmetric skyrmion host material Gd_2PdSi_3 . *Phys. Rev. B* **2023**, *107*, 024405. [[CrossRef](#)]
47. Nomoto, T.; Arita, R. Ab initio exploration of short-pitch skyrmion materials: Role of orbital frustration. *J. Appl. Phys.* **2023**, *133*. [[CrossRef](#)]
48. Hirschberger, M.; Nakajima, T.; Gao, S.; Peng, L.; Kikkawa, A.; Kurumaji, T.; Kriener, M.; Yamasaki, Y.; Sagayama, H.; Nakao, H.; et al. Skyrmion phase and competing magnetic orders on a breathing kagome lattice. *Nat. Commun.* **2019**, *10*, 5831. [[CrossRef](#)]
49. Hirschberger, M.; Hayami, S.; Tokura, Y. Nanometric skyrmion lattice from anisotropic exchange interactions in a centrosymmetric host. *New J. Phys.* **2021**, *23*, 023039. [[CrossRef](#)]
50. Nakamura, S.; Kabeya, N.; Kobayashi, M.; Araki, K.; Katoh, K.; Ochiai, A. Magnetic phases of the frustrated ferromagnetic spin-trimer system $\text{Gd}_3\text{Ru}_4\text{Al}_{12}$ with a distorted kagome lattice structure. *Phys. Rev. B* **2023**, *107*, 014422. [[CrossRef](#)]
51. Ogunbunmi, M.O.; Nair, H.S.; Strydom, A.M. Magnetic frustration-driven ground state properties of rare-earth magnetic ions on a breathing kagome lattice: A review of the $\text{Gd}_3\text{Ru}_4\text{Al}_{12}$ structure type magnets. *Crit. Rev. Solid State Mater. Sci.* **2023**, *48*, 480–501. [[CrossRef](#)]
52. Khanh, N.D.; Nakajima, T.; Yu, X.; Gao, S.; Shibata, K.; Hirschberger, M.; Yamasaki, Y.; Sagayama, H.; Nakao, H.; Peng, L.; et al. Nanometric square skyrmion lattice in a centrosymmetric tetragonal magnet. *Nat. Nanotechnol.* **2020**, *15*, 444. [[CrossRef](#)] [[PubMed](#)]
53. Matsuyama, N.; Nomura, T.; Imajo, S.; Nomoto, T.; Arita, R.; Sudo, K.; Kimata, M.; Khanh, N.D.; Takagi, R.; Tokura, Y.; et al. Quantum oscillations in the centrosymmetric skyrmion-hosting magnet GdRu_2Si_2 . *Phys. Rev. B* **2023**, *107*, 104421. [[CrossRef](#)]
54. Hayami, S.; Kato, Y. Widely-sweeping magnetic field–temperature phase diagrams for skyrmion-hosting centrosymmetric tetragonal magnets. *J. Magn. Magn. Mater.* **2023**, *571*, 170547. [[CrossRef](#)]
55. Wood, G.D.A.; Khalyavin, D.D.; Mayoh, D.A.; Bouaziz, J.; Hall, A.E.; Holt, S.J.R.; Orlandi, F.; Manuel, P.; Blügel, S.; Staunton, J.B.; et al. Double-Q ground state with topological charge stripes in the centrosymmetric skyrmion candidate GdRu_2Si_2 . *Phys. Rev. B* **2023**, *107*, L180402. [[CrossRef](#)]
56. Ereemeev, S.; Glazkova, D.; Poelchen, G.; Kraiker, A.; Ali, K.; Tarasov, A.; Schulz, S.; Kliemt, K.; Chulkov, E.; Stolyarov, V.; et al. Insight into the electronic structure of the centrosymmetric skyrmion magnet GdRu_2Si_2 . *arXiv* **2023**, arXiv:2306.01370.
57. Canepa, F.; Napoletano, M.; Palenzona, A.; Moze, O.; Kockelmann, W. Ferromagnetic and incommensurate antiferromagnetic order in a multi-sublattice itinerant magnet: $\text{Y}_3\text{Co}_8\text{Sn}_4$. *J. Phys. Condens. Matter* **2004**, *17*, 373. [[CrossRef](#)]
58. Takagi, R.; White, J.; Hayami, S.; Arita, R.; Honecker, D.; Rønnow, H.; Tokura, Y.; Seki, S. Multiple- q noncollinear magnetism in an itinerant hexagonal magnet. *Sci. Adv.* **2018**, *4*, eaau3402. [[CrossRef](#)]
59. Mühlbauer, S.; Binz, B.; Jonietz, F.; Pfleiderer, C.; Rosch, A.; Neubauer, A.; Georgii, R.; Böni, P. Skyrmion lattice in a chiral magnet. *Science* **2009**, *323*, 915–919. [[CrossRef](#)]
60. Adams, T.; Mühlbauer, S.; Pfleiderer, C.; Jonietz, F.; Bauer, A.; Neubauer, A.; Georgii, R.; Böni, P.; Keiderling, U.; Everschor, K.; et al. Long-Range Crystalline Nature of the Skyrmion Lattice in MnSi . *Phys. Rev. Lett.* **2011**, *107*, 217206. [[CrossRef](#)]
61. Morikawa, D.; Shibata, K.; Kanazawa, N.; Yu, X.Z.; Tokura, Y. Crystal chirality and skyrmion helicity in MnSi and $(\text{Fe}, \text{Co})\text{Si}$ as determined by transmission electron microscopy. *Phys. Rev. B* **2013**, *88*, 024408. [[CrossRef](#)]
62. Bauer, A.; Garst, M.; Pfleiderer, C. Specific Heat of the Skyrmion Lattice Phase and Field-Induced Tricritical Point in MnSi . *Phys. Rev. Lett.* **2013**, *110*, 177207. [[CrossRef](#)]
63. Wilson, M.N.; Butenko, A.B.; Bogdanov, A.N.; Monchesky, T.L. Chiral skyrmions in cubic helimagnet films: The role of uniaxial anisotropy. *Phys. Rev. B* **2014**, *89*, 094411. [[CrossRef](#)]
64. Yokouchi, T.; Kanazawa, N.; Tsukazaki, A.; Kozuka, Y.; Kikkawa, A.; Taguchi, Y.; Kawasaki, M.; Ichikawa, M.; Kagawa, F.; Tokura, Y. Formation of in-plane skyrmions in epitaxial MnSi thin films as revealed by planar Hall effect. *J. Phys. Soc. Jpn.* **2015**, *84*, 104708. [[CrossRef](#)]

65. Chacon, A.; Bauer, A.; Adams, T.; Rucker, F.; Brandl, G.; Georgii, R.; Garst, M.; Pfliederer, C. Uniaxial Pressure Dependence of Magnetic Order in MnSi. *Phys. Rev. Lett.* **2015**, *115*, 267202. [[CrossRef](#)] [[PubMed](#)]
66. Yu, X.; Kikkawa, A.; Morikawa, D.; Shibata, K.; Tokunaga, Y.; Taguchi, Y.; Tokura, Y. Variation of skyrmion forms and their stability in MnSi thin plates. *Phys. Rev. B* **2015**, *91*, 054411. [[CrossRef](#)]
67. Reiner, M.; Bauer, A.; Leitner, M.; Gigl, T.; Anwand, W.; Butterling, M.; Wagner, A.; Kudejova, P.; Pfliederer, C.; Huguenschmidt, C. Positron spectroscopy of point defects in the skyrmion-lattice compound MnSi. *Sci. Rep.* **2016**, *6*, 29109. [[CrossRef](#)] [[PubMed](#)]
68. Mühlbauer, S.; Kindervater, J.; Adams, T.; Bauer, A.; Keiderling, U.; Pfliederer, C. Kinetic small angle neutron scattering of the skyrmion lattice in MnSi. *New J. Phys.* **2016**, *18*, 075017. [[CrossRef](#)]
69. Nakajima, T.; Oike, H.; Kikkawa, A.; Gilbert, E.P.; Booth, N.; Kakurai, K.; Taguchi, Y.; Tokura, Y.; Kagawa, F.; Arima, T.H. Skyrmion lattice structural transition in MnSi. *Sci. Adv.* **2017**, *3*, e1602562. [[CrossRef](#)] [[PubMed](#)]
70. Meynell, S.A.; Wilson, M.N.; Krycka, K.L.; Kirby, B.J.; Fritzsche, H.; Monchesky, T.L. Neutron study of in-plane skyrmions in MnSi thin films. *Phys. Rev. B* **2017**, *96*, 054402. [[CrossRef](#)]
71. Luo, Y.; Lin, S.Z.; Fobes, D.M.; Liu, Z.; Bauer, E.D.; Betts, J.B.; Migliori, A.; Thompson, J.D.; Janoschek, M.; Maiorov, B. Anisotropic magnetocrystalline coupling of the skyrmion lattice in MnSi. *Phys. Rev. B* **2018**, *97*, 104423. [[CrossRef](#)]
72. Bannenberg, L.J.; Sadykov, R.; Dalgliesh, R.M.; Goodway, C.; Schlagel, D.L.; Lograsso, T.A.; Falus, P.; Lelièvre-Berna, E.; Leonov, A.O.; Pappas, C. Skyrmions and spirals in MnSi under hydrostatic pressure. *Phys. Rev. B* **2019**, *100*, 054447. [[CrossRef](#)]
73. Leishman, A.W.D.; Menezes, R.M.; Longbons, G.; Bauer, E.D.; Janoschek, M.; Honecker, D.; DeBeer-Schmitt, L.; White, J.S.; Sokolova, A.; Milošević, M.V.; et al. Topological energy barrier for skyrmion lattice formation in MnSi. *Phys. Rev. B* **2020**, *102*, 104416. [[CrossRef](#)]
74. Dhital, C.; DeBeer-Schmitt, L.; Young, D.P.; DiTusa, J.F. Unpinning the skyrmion lattice in MnSi: Effect of substitutional disorder. *Phys. Rev. B* **2019**, *99*, 024428. [[CrossRef](#)]
75. Chai, Y.; Lu, P.; Du, H.; Shen, J.; Ma, Y.; Zhai, K.; Wang, L.; Shi, Y.; Li, H.; Wang, W.; et al. Probe of skyrmion phases and dynamics in MnSi via the magnetoelectric effect in a composite configuration. *Phys. Rev. B* **2021**, *104*, L100413. [[CrossRef](#)]
76. Kindervater, J.; Stasinopoulos, I.; Bauer, A.; Haslbeck, F.X.; Rucker, F.; Chacon, A.; Mühlbauer, S.; Franz, C.; Garst, M.; Grundler, D.; et al. Weak Crystallization of Fluctuating Skyrmion Textures in MnSi. *Phys. Rev. X* **2019**, *9*, 041059. [[CrossRef](#)]
77. Soda, M.; Forgan, E.M.; Blackburn, E.; Campillo, E.; Ryukhtin, V.; Hoffmann, I.; Kikkawa, A.; Taguchi, Y.; Yoshizawa, H.; Kawano-Furukawa, H. Asymmetric slow dynamics of the skyrmion lattice in MnSi. *Nat. Phys.* **2023**, *19*, 1476–1481. [[CrossRef](#)]
78. Yu, X.Z.; Onose, Y.; Kanazawa, N.; Park, J.H.; Han, J.H.; Matsui, Y.; Nagaosa, N.; Tokura, Y. Real-space observation of a two-dimensional skyrmion crystal. *Nature* **2010**, *465*, 901–904. [[CrossRef](#)] [[PubMed](#)]
79. Adams, T.; Mühlbauer, S.; Neubauer, A.; Münzer, W.; Jonietz, F.; Georgii, R.; Pedersen, B.; Böni, P.; Rosch, A.; Pfliederer, C. Skyrmion lattice domains in $\text{Fe}_{1-x}\text{Co}_x\text{Si}$. *J. Phys. Conf. Ser.* **2010**, *200*, 032001. [[CrossRef](#)]
80. Münzer, W.; Neubauer, A.; Adams, T.; Mühlbauer, S.; Franz, C.; Jonietz, F.; Georgii, R.; Böni, P.; Pedersen, B.; Schmidt, M.; et al. Skyrmion lattice in the doped semiconductor $\text{Fe}_{1-x}\text{Co}_x\text{Si}$. *Phys. Rev. B* **2010**, *81*, 041203. [[CrossRef](#)]
81. Bauer, A.; Garst, M.; Pfliederer, C. History dependence of the magnetic properties of single-crystal $\text{Fe}_{1-x}\text{Co}_x\text{Si}$. *Phys. Rev. B* **2016**, *93*, 235144. [[CrossRef](#)]
82. Dhital, C.; DiTusa, J.F. Entropic signatures of the skyrmion lattice phase in $\text{MnSi}_{1-x}\text{Al}_x$ and $\text{Fe}_{1-y}\text{Co}_y\text{Si}$. *Phys. Rev. B* **2020**, *102*, 224408. [[CrossRef](#)]
83. Kakihana, M.; Aoki, D.; Nakamura, A.; Honda, F.; Nakashima, M.; Amako, Y.; Nakamura, S.; Sakakibara, T.; Hedo, M.; Nakama, T.; et al. Giant Hall resistivity and magnetoresistance in cubic chiral antiferromagnet EuPtSi. *J. Phys. Soc. Jpn.* **2018**, *87*, 023701. [[CrossRef](#)]
84. Kaneko, K.; Frontzek, M.D.; Matsuda, M.; Nakao, A.; Munakata, K.; Ohhara, T.; Kakihana, M.; Haga, Y.; Hedo, M.; Nakama, T.; et al. Unique Helical Magnetic Order and Field-Induced Phase in Trillium Lattice Antiferromagnet EuPtSi. *J. Phys. Soc. Jpn.* **2019**, *88*, 013702. [[CrossRef](#)]
85. Tabata, C.; Matsumura, T.; Nakao, H.; Michimura, S.; Kakihana, M.; Inami, T.; Kaneko, K.; Hedo, M.; Nakama, T.; Ōnuki, Y. Magnetic Field Induced Triple- q Magnetic Order in Trillium Lattice Antiferromagnet EuPtSi Studied by Resonant X-ray Scattering. *J. Phys. Soc. Jpn.* **2019**, *88*, 093704. [[CrossRef](#)]
86. Kakihana, M.; Aoki, D.; Nakamura, A.; Honda, F.; Nakashima, M.; Amako, Y.; Takeuchi, T.; Harima, H.; Hedo, M.; Nakama, T.; et al. Unique Magnetic Phases in the Skyrmion Lattice and Fermi Surface Properties in Cubic Chiral Antiferromagnet EuPtSi. *J. Phys. Soc. Jpn.* **2019**, *88*, 094705. [[CrossRef](#)]
87. Mishra, A.K.; Ganesan, V. A-phase, field-induced tricritical point, and universal magnetocaloric scaling in EuPtSi. *Phys. Rev. B* **2019**, *100*, 125113. [[CrossRef](#)]
88. Takeuchi, T.; Kakihana, M.; Hedo, M.; Nakama, T.; Ōnuki, Y. Magnetic field versus temperature phase diagram for $\text{H}||[001]$ in the trillium lattice antiferromagnet EuPtSi. *J. Phys. Soc. Jpn.* **2019**, *88*, 053703. [[CrossRef](#)]

89. Sakakibara, T.; Nakamura, S.; Kittaka, S.; Kakihana, M.; Hedo, M.; Nakama, T.; Ōnuki, Y. Fluctuation-Induced First-Order Transition and Tricritical Point in EuPtSi. *J. Phys. Soc. Jpn.* **2019**, *88*, 093701. [[CrossRef](#)]
90. Takeuchi, T.; Kakihana, M.; Hedo, M.; Nakama, T.; Ōnuki, Y. Angle Dependence of the Magnetic Phase Diagram in Cubic Chiral Antiferromagnet EuPtSi. *J. Phys. Soc. Jpn.* **2020**, *89*, 093703. [[CrossRef](#)]
91. Hayami, S.; Yambe, R. Field-Direction Sensitive Skyrmion Crystals in Cubic Chiral Systems: Implication to 4f-Electron Compound EuPtSi. *J. Phys. Soc. Jpn.* **2021**, *90*, 073705. [[CrossRef](#)]
92. Sakakibara, T.; Nakamura, S.; Kittaka, S.; Kakihana, M.; Hedo, M.; Nakama, T.; Onuki, Y. Magnetic Phase Transitions of the 4f Skyrmion Compound EuPtSi Studied by Magnetization Measurements. *J. Phys. Soc. Jpn.* **2021**, *90*, 064701. [[CrossRef](#)]
93. Goetsch, R.J.; Anand, V.K.; Johnston, D.C. Antiferromagnetism in EuNiGe₃. *Phys. Rev. B* **2013**, *87*, 064406. [[CrossRef](#)]
94. Fabrèges, X.; Gukasov, A.; Bonville, P.; Maurya, A.; Thamizhavel, A.; Dhar, S.K. Exploring metamagnetism of single crystalline EuNiGe₃ by neutron scattering. *Phys. Rev. B* **2016**, *93*, 214414. [[CrossRef](#)]
95. Singh, D.; Fujishiro, Y.; Hayami, S.; Moody, S.H.; Nomoto, T.; Baral, P.R.; Ukleev, V.; Cubitt, R.; Steinke, N.J.; Gawryluk, D.J.; et al. Transition between distinct hybrid skyrmion textures through their hexagonal-to-square crystal transformation in a polar magnet. *Nat. Commun.* **2023**, *14*, 8050. [[CrossRef](#)]
96. Matsumura, T.; Kurauchi, K.; Tsukagoshi, M.; Higa, N.; Nakao, H.; Kakihana, M.; Hedo, M.; Nakama, T.; Ōnuki, Y. Distorted triangular skyrmion lattice in a noncentrosymmetric tetragonal magnet. *arXiv* **2023**, arXiv:2306.14767.
97. Rößler, U.K.; Bogdanov, A.N.; Pfleiderer, C. Spontaneous skyrmion ground states in magnetic metals. *Nature* **2006**, *442*, 797–801. [[CrossRef](#)] [[PubMed](#)]
98. Yi, S.D.; Onoda, S.; Nagaosa, N.; Han, J.H. Skyrmions and anomalous Hall effect in a Dzyaloshinskii-Moriya spiral magnet. *Phys. Rev. B* **2009**, *80*, 054416. [[CrossRef](#)]
99. Hayami, S.; Motome, Y. Effect of magnetic anisotropy on skyrmions with a high topological number in itinerant magnets. *Phys. Rev. B* **2019**, *99*, 094420. [[CrossRef](#)]
100. Hayami, S.; Motome, Y. Noncoplanar multiple-Q spin textures by itinerant frustration: Effects of single-ion anisotropy and bond-dependent anisotropy. *Phys. Rev. B* **2021**, *103*, 054422. [[CrossRef](#)]
101. Yambe, R.; Hayami, S. Effective spin model in momentum space: Toward a systematic understanding of multiple-Q instability by momentum-resolved anisotropic exchange interactions. *Phys. Rev. B* **2022**, *106*, 174437. [[CrossRef](#)]
102. Hayami, S.; Motome, Y. Néel- and Bloch-Type Magnetic Vortices in Rashba Metals. *Phys. Rev. Lett.* **2018**, *121*, 137202. [[CrossRef](#)] [[PubMed](#)]
103. Ruderman, M.A.; Kittel, C. Indirect Exchange Coupling of Nuclear Magnetic Moments by Conduction Electrons. *Phys. Rev.* **1954**, *96*, 99–102. [[CrossRef](#)]
104. Kasuya, T. A Theory of Metallic Ferro- and Antiferromagnetism on Zener's Model. *Prog. Theor. Phys.* **1956**, *16*, 45–57. [[CrossRef](#)]
105. Yosida, K. Magnetic Properties of Cu-Mn Alloys. *Phys. Rev.* **1957**, *106*, 893–898. [[CrossRef](#)]
106. Shekhtman, L.; Aharony, A.; Entin-Wohlman, O. Bond-dependent symmetric and antisymmetric superexchange interactions in La₂CuO₄. *Phys. Rev. B* **1993**, *47*, 174–182. [[CrossRef](#)]
107. Khomskii, D.; Mostovoy, M. Orbital ordering and frustrations. *J. Phys. A* **2003**, *36*, 9197. [[CrossRef](#)]
108. Jackeli, G.; Khaliullin, G. Mott insulators in the strong spin-orbit coupling limit: From Heisenberg to a quantum compass and Kitaev models. *Phys. Rev. Lett.* **2009**, *102*, 017205. [[CrossRef](#)]
109. Li, Y.D.; Wang, X.; Chen, G. Anisotropic spin model of strong spin-orbit-coupled triangular antiferromagnets. *Phys. Rev. B* **2016**, *94*, 035107. [[CrossRef](#)]
110. Maksimov, P.A.; Zhu, Z.; White, S.R.; Chernyshev, A.L. Anisotropic-Exchange Magnets on a Triangular Lattice: Spin Waves, Accidental Degeneracies, and Dual Spin Liquids. *Phys. Rev. X* **2019**, *9*, 021017. [[CrossRef](#)]
111. Becker, M.; Hermanns, M.; Bauer, B.; Garst, M.; Trebst, S. Spin-orbit physics of $j = \frac{1}{2}$ Mott insulators on the triangular lattice. *Phys. Rev. B* **2015**, *91*, 155135. [[CrossRef](#)]
112. Rouschatzakis, I.; Rössler, U.K.; van den Brink, J.; Daghofer, M. Kitaev anisotropy induces mesoscopic Z₂ vortex crystals in frustrated hexagonal antiferromagnets. *Phys. Rev. B* **2016**, *93*, 104417. [[CrossRef](#)]
113. Liu, C.; Yu, R.; Wang, X. Semiclassical ground-state phase diagram and multi-Q phase of a spin-orbit-coupled model on triangular lattice. *Phys. Rev. B* **2016**, *94*, 174424. [[CrossRef](#)]
114. Chern, G.W.; Sizyuk, Y.; Price, C.; Perkins, N.B. Kitaev-Heisenberg model in a magnetic field: Order-by-disorder and commensurate-incommensurate transitions. *Phys. Rev. B* **2017**, *95*, 144427. [[CrossRef](#)]
115. Hayami, S.; Yambe, R. Degeneracy Lifting of Néel, Bloch, and Anti-Skyrmion Crystals in Centrosymmetric Tetragonal Systems. *J. Phys. Soc. Jpn.* **2020**, *89*, 103702. [[CrossRef](#)]
116. Kamiya, Y.; Batista, C.D. Magnetic Vortex Crystals in Frustrated Mott Insulator. *Phys. Rev. X* **2014**, *4*, 011023. [[CrossRef](#)]
117. Hayami, S.; Lin, S.Z.; Kamiya, Y.; Batista, C.D. Vortices, skyrmions, and chirality waves in frustrated Mott insulators with a quenched periodic array of impurities. *Phys. Rev. B* **2016**, *94*, 174420. [[CrossRef](#)]
118. Hayami, S. In-plane magnetic field-induced skyrmion crystal in frustrated magnets with easy-plane anisotropy. *Phys. Rev. B* **2021**, *103*, 224418. [[CrossRef](#)]
119. Chandragiri, V.; Iyer, K.K.; Sampathkumaran, E. Magnetic behavior of Gd₃Ru₄Al₁₂, a layered compound with distorted kagomé net. *J. Phys. Condens. Matter* **2016**, *28*, 286002. [[CrossRef](#)]

120. Nakamura, S.; Kabeya, N.; Kobayashi, M.; Araki, K.; Katoh, K.; Ochiai, A. Spin trimer formation in the metallic compound $Gd_3Ru_4Al_{12}$ with a distorted kagome lattice structure. *Phys. Rev. B* **2018**, *98*, 054410. [[CrossRef](#)]
121. Matsumura, T.; Ozono, Y.; Nakamura, S.; Kabeya, N.; Ochiai, A. Helical ordering of spin trimers in a distorted kagome lattice of $Gd_3Ru_4Al_{12}$ studied by resonant x-ray diffraction. *J. Phys. Soc. Jpn.* **2019**, *88*, 023704. [[CrossRef](#)]

Disclaimer/Publisher's Note: The statements, opinions and data contained in all publications are solely those of the individual author(s) and contributor(s) and not of MDPI and/or the editor(s). MDPI and/or the editor(s) disclaim responsibility for any injury to people or property resulting from any ideas, methods, instructions or products referred to in the content.